

Model-Based Control for Ultrasonic Motors

Jürgen Maas, Thomas Schulte, and Norbert Fröhleke

Abstract—A complete model-based control for traveling-wave-type ultrasonic motors is presented in this paper. The control scheme consists of inner control loops with respect to the oscillation systems, offering all meaningful degrees of freedom for adjusting the traveling bending wave, and outer control loops for torque and speed. After a brief review on modeling the actuator and presentation of a parameter identification method, the control scheme is developed and verified by measurements on a prototype drive system. Several measures for the compensation of nonlinearities and temperature effects are developed and achieved improvements are discussed with respect to the special properties of this novel actuator. Finally the developed drive is applied to an “active control stick.”

Index Terms—Active control stick, motion control, nonlinear oscillation systems, piezoelectric ultrasonic motors, vibration control.

I. INTRODUCTION

PIEZOELECTRIC ultrasonic motors (USM's) have attracted considerable attention as a new type of actuator for servo drive applications, e.g., as actuators for robotics. In particular, rotary traveling-wave-type USM's combine features such as high driving torque at low rotational speed, high holding torque, low electromagnetic interference, and are also more compact than conventional geared motors.

Fig. 1(a) shows an exploded view of a rotary traveling-wave-type USM with its basic components. The driving principle [1] is based on a two-stage energy conversion process.

In the first energy conversion stage, mechanical vibrations of the stator are excited to its eigenfrequency by a ring-shaped piezoelectric ceramic actuator which is bonded to the “lower surface” of the stator. The piezoelectric ceramic ring is divided into two excitation systems (two phases) whose sectors are alternately positively and negatively polarized. Each system is fed by a sinusoidal voltage in the ultrasonic range (40–45 kHz) generating a standing wave on the stator [see Fig. 1(b)]. Since a spatial phase shift of a quarter wave length is introduced between the excitation systems, a traveling bending wave is generated by a correct superposition of both standing waves achieved with proper amplitudes and a well-defined temporal phase shift.

The rotor is pressed against the stator by means of a disc spring. In most traveling-wave motors, the rotor is coated with a special lining material, realized by an elastic contact layer,

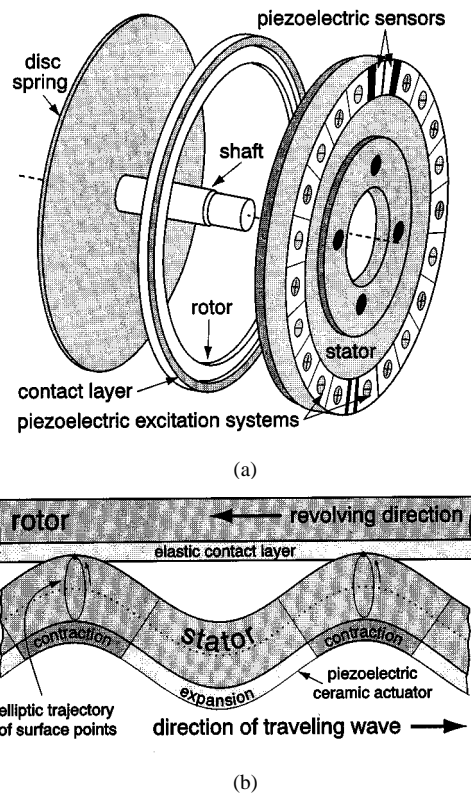


Fig. 1. (a) Basic components of rotary traveling-wave-type USM. (b) Driving principle of traveling-wave-type USM.

in order to obtain good force transmission [see Fig. 1(b)]. Due to the traveling bending wave, the surface points of the stator perform elliptic motions containing a vertical and a horizontal component. While a normal pressure distribution is produced at each wave crest by the vertical movement, frictional force is generated inside the elastic contact layer driving the rotor by the horizontal movement. This second energy conversion stage is characterized by extreme nonlinear contact mechanism between stator and rotor.

Due to the complex and nonlinear characteristics of USM's, intensive research efforts are required to optimize the performance of USM's. Besides several research activities with respect to the motor design and materials, an appropriate drive control must be applied for sufficient operation, since the motor parameters are influenced heavily by temperature (e.g., mechanical eigenfrequency and speed characteristic; see, also, [2]). The behavior of the motor is characterized by a nonlinear mechanical oscillation system and nonlinear torque generation (see Sections II-D and V-B) [3].

Several control strategies have been proposed, which are based on black-box modeling and fuzzy or neuro methods [4], [5]. Since these control schemes are developed without any

Manuscript received December 15, 1999; revised February 1, 2000. This work was supported by the Deutsche Forschungs Gemeinschaft (DFG).

J. Maas was with the Institute for Power Electronics and Electrical Drives, University of Paderborn, D-33098 Paderborn, Germany. He is now with DaimlerChrysler AG Research and Technology, D-60528 Frankfurt, Germany (e-mail: juergen.maas@daimlerchrysler.com).

T. Schulte and N. Fröhleke are with the Institute for Power Electronics and Electrical Drives, University of Paderborn, D-33098 Paderborn, Germany (e-mail: schulte@lea.uni-paderborn.de).

Publisher Item Identifier S 1083-4435(00)05159-0.

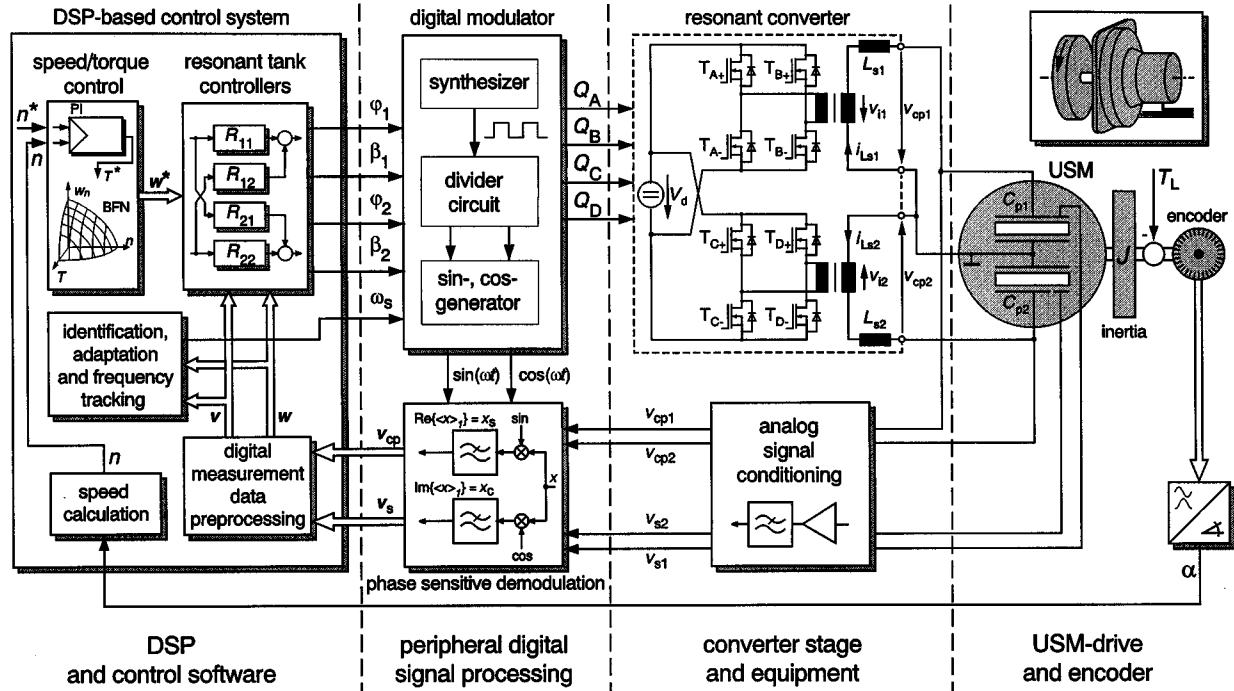


Fig. 2. Overall scheme of the developed USM-drive system.

analytical model approach, their potential of optimization is limited. They neglect decisive nonlinearities and motor asymmetries and make use of frequency modulation to adjust the speed. Consequently, the well-known pullout phenomenon (see Section IV-C) of USM's occurs, by which a large advantageous range of the drive's performance cannot be utilized.

In the following, a complete model-based control scheme is presented which avoids the latter disadvantages. Fig. 2 shows the overall scheme of the developed drive system, with details being explained in [7]. The electrical excitation of motor vibrations is applied by a specially designed two-phase voltage-source converter. Due to dielectric properties of the piezoelectric ceramic, characterized by a capacitance in each phase, inductors L_{s1} and L_{s2} have to be added in series. Thus, the USM becomes an integral part of a resonant converter. Two small sectors of the piezoelectric ceramic layer (see Fig. 1) are utilized for detecting both standing waves denoted by sensor signals v_{s1} (assigned to phase 1) and v_{s2} (assigned to phase 2). In order to deal with the motor asymmetries and cross couplings caused by the piezoelectric ceramic layer and the vibrating stator, the feeding full-bridge inverter stage is driven by adequate control quantities which guarantee all necessary degrees of freedom: switching frequency $\omega_s = 2\pi \cdot f_s$, phase angles φ_1 and φ_2 , as well as duty cycles β_1 and β_2 of both phases (see Fig. 3). These control quantities enable an independent adjustment of voltage amplitudes and phases to obtain optimized motor conditions. The measurements in Fig. 3 illustrate that the USM must be fed by different voltage amplitudes and an electrical phase shift which differs from 90° in order to compensate motor asymmetries for optimized conditions. The corresponding driving signals Q_A , Q_B , Q_C , Q_D of the transistors are generated by a digital modulator controlled by a digital signal processor (DSP).

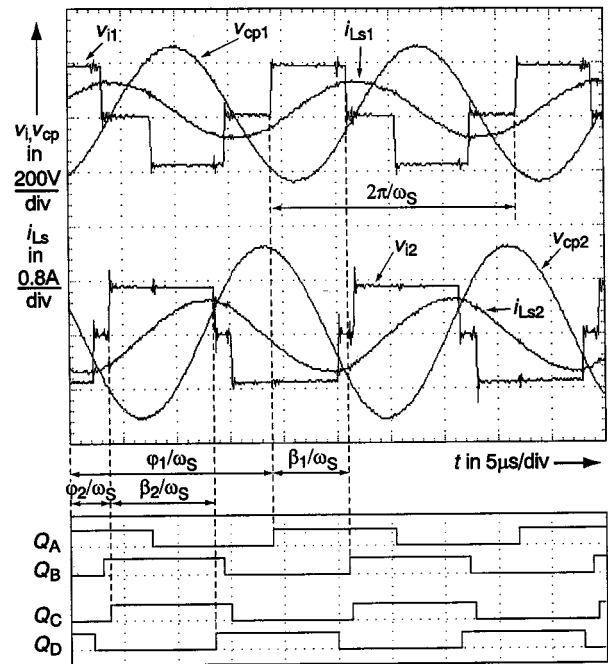


Fig. 3. Measured voltages $v_{Cp1,2}$ and currents $i_{Ls1,2}$ of USM and measured output voltage $v_{i1,2}$ of inverter stage resulting from modulator signals Q_A , Q_B , Q_C , and Q_D set by control values ω_s , φ_1 , φ_2 , β_1 , and β_2 .

As shown by measured electrical state variables in Fig. 3, the quantities of the electrical and mechanical resonant circuits are characterized by sinusoidal waveforms in the ultrasonic frequency range. Only the fundamental components of motor voltages v_{cp} and sensor signals v_s are used as feedback informa-

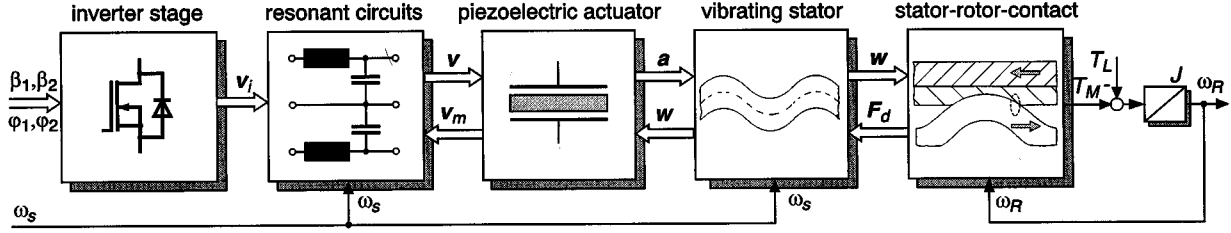


Fig. 4. Simulation model of converter-fed ultrasonic motor divided into its functional modules.

tion for control which are determined by analog phase-sensitive demodulation circuits. Additionally, the position of the rotor is detected by an incremental encoder.

The block named “DSP-based control system” is focused on in this paper. The main goal is a speed-controlled USM drive offering high performance for servo applications as required for an “active control stick,” presented in Section VI. Since the bending wave is decisive for the torque generation (comparable with the current of conventional electrical motors), it seems to be meaningful to apply inner controls for the electrical and mechanical oscillation systems. Their design is described in Section IV. The inner controls consider compensation measures for asymmetries and cross couplings and the pullout phenomenon is avoided by using amplitude modulation instead of frequency modulation. Thus, the motor can be operated at the mechanical resonance optimizing the drives performance remarkably. By means of an inverse contact model, the nonlinear torque generation is compensated. Therefore, an open-loop torque control is applicable such that proven speed control schemes can be implemented as discussed in Section V. First, a brief review on modeling is given in Section II and a parameter identification method is proposed in Section III.

II. MODEL OF INVERTER-FED USM

USM's are characterized by a two-stage energy conversion process as previously explained. By the conversion process, the energy is transferred from electrical input to mechanical output terminals using different types of functional modules summarized in Fig. 4. Since the modules consist of electrical as well as mechanical components, the new actuator represents a typical example of a mechatronic system completed by a control for envisaged operation mode and performance. While the electrical and mechanical oscillation systems can be described by linear transfer properties, the piezoelectric energy conversion and the micromechanical contact between stator and rotor are characterized by nonlinear behavior. Appropriate models are essential for optimization of the overall drive performance and designing the control. The simulation model derived in [8] describes the total drive system by combining the electrical and mechanical partial models as indicated in Fig. 4. On one hand, the simulation model reflects the ultrasonic oscillations (see Fig. 3) of the electrical and mechanical resonant circuits and is, therefore, indispensable for detailed studies of the motor performance. However, on the other hand, this so-called *original model* cannot be used straightforward when designing the control, because am-

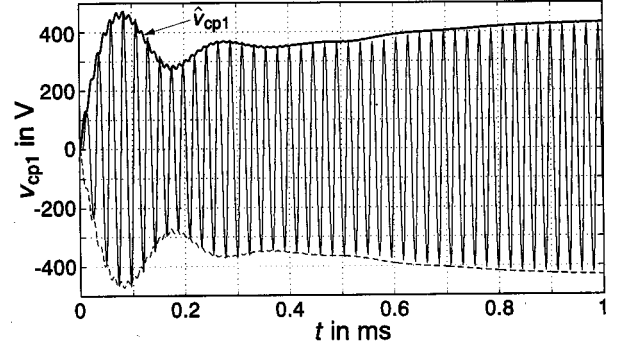


Fig. 5. Comparison between original model and averaged model for motor voltage v_{cp1} .

plitudes and phases of the ultrasonic oscillations can only be influenced by the control signals ω_s , φ_1 , φ_2 , β_1 , and β_2 .

In order to obtain an appropriate model for the control design, an averaged model is derived in [10] based on the original model in [8]. Since this paper deals with the design of the drive control, essential details of the averaged model are selected to be described in the following. According to the resonant structures, the ultrasonic oscillations contain a major fundamental component shown by measurements in Fig. 3. The sinusoidal waveform of each ultrasonic oscillation can be well approximated by

$$x(t) = x_s(t) \sin(\omega t) + x_c(t) \cos(\omega t). \quad (1)$$

The averaged model in [10] reflects the slow dynamic behavior of the fast-changing ultrasonic oscillations $x(t)$ using their time-varying fundamental Fourier coefficients $x_s(t)$ and $x_c(t)$ (in Cartesian coordinates) as new state quantities and is, thus, predestined for designing the control.

In Fig. 5, a comparison between simulation results obtained by the original and averaged model are illustrated for motor voltage v_{cp1} . Since the envelope of the ultrasonic oscillation $v_{cp1}(t)$ is well approximated by the amplitude $\hat{v}_{cp1}(t)$, calculated by the state variables of the averaged model through

$$\hat{v}_{cp1} = \sqrt{v_{cp1s}^2 + v_{cp1c}^2}, \quad (2)$$

the results verify the selected approach based on the averaging method.

A. Model of Electrical Subsystem

The electrical subsystem comprises the inverter stage and the electrical resonant tanks represented by the series inductances

L_{s1} , L_{s2} of the converter and the capacitances C_{p1} , C_{p2} of the piezoelectric ceramic (see Fig. 2), taking losses of the components additionally into account. Inputs of the resonant circuits are the fundamental voltage components of the inverter stage

$$\mathbf{v}_i^T = [v_{i1s} \quad v_{i1c} \quad v_{i2s} \quad v_{i2c}] \quad (3)$$

resulting from control inputs ω_s , φ_1 , φ_2 , β_1 , and β_2 of the two-phase resonant converter. The output quantities are given by the vector of fundamental model voltages

$$\mathbf{v}^T = [v_{1s} \quad v_{1c} \quad v_{2s} \quad v_{2c}]. \quad (4)$$

The dynamic behavior between input voltage \mathbf{v}_i and output voltage \mathbf{v} is given by the transfer matrix

$$\mathbf{G}_{el}(s) = \begin{bmatrix} G_{Del}(s) & G_{Cel}(s) \\ -G_{Cel}(s) & G_{Del}(s) \end{bmatrix} \quad (5)$$

using indexes 1 and 2 for the two-phase model of the electrical subsystem

$$\mathbf{v} = \begin{bmatrix} \mathbf{G}_{el1} & 0 \\ 0 & \mathbf{G}_{el2} \end{bmatrix} (\mathbf{v}_i + \mathbf{v}_m). \quad (6)$$

\mathbf{v}_m describes the feedback of the vibrating stator on the feeding converter by the piezoelectric effect (see Section II-B). Each phase is characterized by a multivariable plant \mathbf{G}_{el} denoted by transfer function G_{Del} for direct dynamical couplings between the time-varying Fourier coefficients and denoted by transfer functions G_{Cel} for dynamical cross couplings. For the control design these transfer functions can be reduced to second-order models, containing the eigenvalues $-\delta_{el} \pm j(\omega_s - \omega_{el}) = -\delta_{el} \pm j\Delta\omega_{el}$, as outlined in [11] given by

$$G_{Del} = \frac{\omega_{el}^2(\delta_{el}^2 + \omega_{el}^2 - \omega_s^2)}{(\delta_{el}^2 + (\omega_s + \omega_{el})^2)(\delta_{el}^2 + (\omega_s - \omega_{el})^2)} \cdot \frac{\delta_{el}^2 + (\omega_s - \omega_{el})^2}{s^2 + 2\delta_{el}s + \delta_{el}^2 + (\omega_s - \omega_{el})^2} \quad (7)$$

$$G_{Cel} = \frac{2\omega_s\omega_{el}^2\delta_{el}}{(\delta_{el}^2 + (\omega_s + \omega_{el})^2)(\delta_{el}^2 + (\omega_s - \omega_{el})^2)} \cdot \frac{(\delta_{el}^2 + (\omega_s - \omega_{el})^2)(s + \delta_{el})}{(s^2 + 2\delta_{el}s + \delta_{el}^2 + (\omega_s - \omega_{el})^2)\delta_{el}}. \quad (8)$$

B. Piezoelectric Energy Conversion Process

The motor voltages excite the mechanical subsystem of the stator via the inverse piezoelectric effect. Usually, a scalar and linear approach is used for describing the piezoelectric ceramic actuator. In [6], a model for a piezoelectric stack actuator was derived and it was proven successfully by measurements. A Maxwell resistive capacitance (MRC) was introduced in the electrical subsystem in series [Fig. 6(a)]. Its behavior is given by a rate-independent hysteresis between stored charge q and applied voltage v_{MRC} [Fig. 6(b)], while the behavior of the block

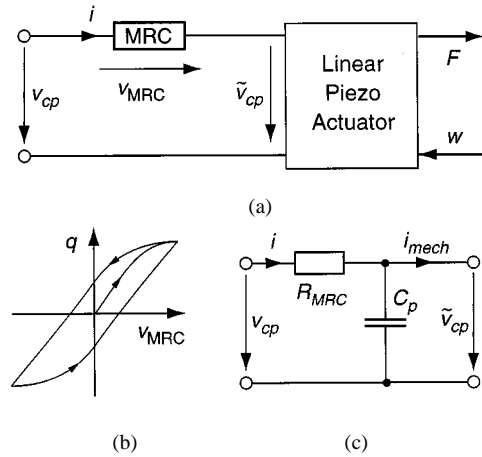


Fig. 6. MRC. (a) Model of piezoelectric actuator with MRC element. (b) Rate independent hysteresis of MRC element. (c) Equivalent circuit of the piezoelectric actuator with MRC.

linear piezo actuator is described by linear properties. Since no specific boundary conditions are given, this model is used as an appropriate model approach for piezoelectric motors. For a detailed elaboration of the model refinement, see [15].

With respect to the averaged model, the describing function of the MRC contains a real and an imaginary part because of its hysteresis. Within a small operation range, it can be described by series-connected linear capacitance C_{MRC} and resistance R_{MRC} . Since it is not possible to distinguish between C_{MRC} and the total piezoelectric capacitance C_p , C_p is considered only as illustrated by the equivalent electric circuit in Fig. 6(c).

The voltage drop across R_{MRC} in Fig. 6 lowers the effective voltage \tilde{v}_{cp} in comparison to measurable motor voltage v_{cp} . In equation (4), model voltages \mathbf{v} are introduced in order to obtain a simple model structure describing the electrical oscillation system without impact of the mechanical oscillation system. Therefore, piezoelectric feedback voltages \mathbf{v}_m must be introduced on one hand in (6) as additional inputs (see Fig. 4). On the other hand, feedback voltages \mathbf{v}_m and R_{MRC} must be taken into account when calculating \mathbf{v} from measurable motor voltages \mathbf{v}_{cp} , too. \mathbf{v} is given by (9), shown at the bottom of the next page. Voltage vector \mathbf{v} excites the mechanical subsystem by acceleration vector

$$\mathbf{a} = \begin{bmatrix} a_{1s} \\ a_{1c} \\ a_{2s} \\ a_{2c} \end{bmatrix} = \frac{1}{m} \begin{bmatrix} A_1 & 0 & A_2\varepsilon_1 & 0 \\ 0 & A_1 & 0 & A_2\varepsilon_1 \\ A_1\varepsilon_2 & 0 & A_2 & 0 \\ 0 & A_1\varepsilon_2 & 0 & A_2 \end{bmatrix} \mathbf{v} - \mathbf{a}_w = \mathbf{K}_{pv}\mathbf{v} - \mathbf{a}_w. \quad (10)$$

m represents the modal mass of vibrating stator, \mathbf{K}_{pv} contains the electromechanical coupling by coefficients A_1 , A_2 , and term \mathbf{a}_w models small direct cross couplings between the mechanical modes (for details refer to [11]). Due to inaccuracies when manufactured and inhomogenities when bonding, the piezoelectric actuator cross excitation of the two-phase piezoelectric actuator must be taken into account considered by coefficients ε_1 , ε_2 in matrix \mathbf{K}_{pv} .

Reflecting the general principle of the electromechanical energy conversion, piezoelectric feedback voltages \mathbf{v}_m are calculated by

$$\begin{aligned} \mathbf{v}_m &= \begin{bmatrix} v_{m1s} \\ v_{m1c} \\ v_{m2s} \\ v_{m2c} \end{bmatrix} \\ &= \begin{bmatrix} A_1/C_{p1} & 0 & A_1\varepsilon_2/C_{p1} & 0 \\ 0 & A_1/C_{p1} & 0 & A_1\varepsilon_2/C_{p1} \\ A_2\varepsilon_1/C_{p2} & 0 & A_2/C_{p2} & 0 \\ 0 & A_2\varepsilon_1/C_{p2} & 0 & A_2/C_{p2} \end{bmatrix} \\ &\quad \cdot \begin{bmatrix} w_{1s} \\ w_{1c} \\ w_{2s} \\ w_{2c} \end{bmatrix} \\ &= \mathbf{K}_{pw} \mathbf{w} \end{aligned} \quad (11)$$

with matrix \mathbf{K}_{pw} containing transposed \mathbf{K}_{pv} and capacitances C_{p1} , C_{p2} of the piezoelectric actuator. Vector \mathbf{w} represents the fundamental components of the traveling bending wave in the averaged model.

C. Model of Vibrating Stator

The dynamics of the vibrating stator are well modeled by a two-mass approximation describing both standing waves under consideration of asymmetries by a small difference with respect to their eigenfrequencies. The dynamic transfer behavior of the averaged model between input quantity \mathbf{a} and output quantity \mathbf{w} is given by

$$\mathbf{w} = \begin{bmatrix} \mathbf{G}_{m1} & 0 \\ 0 & \mathbf{G}_{m2} \end{bmatrix} \cdot \mathbf{a}. \quad (12)$$

Using indexes 1 and 2 for both standing waves, the transfer matrix

$$\mathbf{G}_m(s) = \begin{bmatrix} G_{Dm}(s) & G_{Cm}(s) \\ -G_{Cm}(s) & G_{Dm}(s) \end{bmatrix} \quad (13)$$

models the multivariable plant properties of one mechanical resonant tank. By simplification of the transfer functions above, second-order models are obtained containing the eigenvalues $-\delta_m \pm j(\omega_s - \omega_m) = -\delta_m \pm j\Delta\omega_m$

$$\begin{aligned} G_{Dm} &= \frac{\delta_m^2 + \omega_m^2 - \omega_s^2}{(\delta_m^2 + (\omega_s + \omega_m)^2)(\delta_m^2 + (\omega_s - \omega_m)^2)} \\ &\quad \cdot \frac{\delta_m^2 + (\omega_s - \omega_m)^2}{s^2 + 2\delta_m s + \delta_m^2 + (\omega_s - \omega_m)^2} \end{aligned} \quad (14)$$

$$\begin{aligned} G_{Cm} &= \frac{2\omega_s \delta_m}{(\delta_m^2 + (\omega_s + \omega_m)^2)(\delta_m^2 + (\omega_s - \omega_m)^2)} \\ &\quad \cdot \frac{(\delta_m^2 + (\omega_s - \omega_m)^2)(s + \delta_m)}{(s^2 + 2\delta_m s + \delta_m^2 + (\omega_s - \omega_m)^2)\delta_m}. \end{aligned} \quad (15)$$

D. Nonlinear Stator–Rotor Contact Mechanism and Rotor Model

Modeling the friction mechanism, an elastic model for the contact layer is applied in [8], describing the nonlinear interaction between the models of stator and rotor. The contact model is derived for the general case of a nonperfect traveling wave, which means in comparison to a perfect traveling wave that, in this case, the amplitudes of both standing waves are dissimilar and/or the temporal phase shift between them differs from 90° . Feedback impacts of contact forces on the stator are modeled by a modal forcing vector \mathbf{F}_d . Contact forces acting on the rotor are described by motor torque T_M opposing the applied load torque T_L . Modeling the rotor dynamics the drive's speed $\omega_R = \pi/30$ (s/r/min) $\cdot n$ is taken into account by the model given in Fig. 4. For the control design, a one-mass system is assumed represented by inertia J . Under consideration of averaging method for the vibrating stator, the fundamental describing functions of \mathbf{F}_d are of interest only, while for the rotor dynamic, the dc value of T_M is important.

The eigenvalues of the mechanical vibrator are affected by the nonlinear impacts of contact forces \mathbf{F}_d . The viscoelastic properties of the contact layer and the feedback of frictional forces cause, on one hand, an increase of total stiffness of the vibrating system by which a shift of the vibrator's eigenfrequency ω_m of about $2\pi \cdot 2$ kHz results. On the other hand the vibration's damping increases, yielding variations of coefficient δ_m .

Under consideration of contact forces, the vibrating system reflects a nonlinear large signal model, whose eigenvalues depend strongly on the operating point (in particular, on the amplitude \hat{w} of the traveling bending wave). However, an online calculation of \mathbf{F}_d for control measures is not feasible due to the complex nonlinear characteristic, which requires high computation demands. Moreover, the practicability failed, too, because of inaccuracy of the contact model and uncertainties of parameters caused by temperature effects. Therefore, an alternative solution is proposed to obtain optimized drive performance under consideration of the nonlinear feedback. As is commonly known, such systems can be treated by linearization at the operating point and an adaptive control with respect to the operating point.

Besides the variations of eigenvalues by contact forces, the influence of switching frequency ω_s must be considered, too. This has an impact on the dynamics of the oscillation systems. As indicated by the signal line for ω_s in Fig. 4, the switching

$$\mathbf{v} = \begin{bmatrix} 1 & -R_{MRC}C_p\omega_s & 0 & 0 \\ R_{MRC}C_p\omega_s & 1 & 0 & 0 \\ 0 & 0 & 1 & -R_{MRC}C_p\omega_s \\ 0 & 0 & R_{MRC}C_p\omega_s & 1 \end{bmatrix} \cdot (\mathbf{v}_{cp} + \mathbf{v}_m) \quad (9)$$

frequency is varied by the control during operation. Thus, the small-signal behavior of the stator model is derived by linearization in case of small disturbances of $\Delta\tilde{\omega}_m$, $\Delta\delta_m$, and $\Delta\omega_s$. After suitable simplifications, [11], the linearized stator model at the operating point P is obtained by

$$\begin{bmatrix} W_s(s) \\ W_c(s) \end{bmatrix} = \mathbf{G}_m(s) \left(\begin{bmatrix} A_s(s) \\ A_c(s) \end{bmatrix} + 2\omega_{s,P} \begin{bmatrix} w_{s,P} & w_{c,P} \\ w_{c,P} & -w_{s,P} \end{bmatrix} \cdot \begin{bmatrix} \Delta\omega_s(s) - \Delta\tilde{\omega}_m(s) \\ \Delta\delta_m(s) \end{bmatrix} \right). \quad (16)$$

As indicated by (16), impact on the bending wave \mathbf{w} caused by the discussed disturbances are described by the same transfer matrix \mathbf{G}_m as derived in (13). Thus, a small frequency modulation can be approximated by an amplitude modulation. Moreover, effects of disturbance $\Delta\tilde{\omega}_m$ can be eliminated by adequate frequency modulation of $\Delta\omega_s$ (see Section IV-B).

Besides the nonlinear impacts analyzed above, slow-varying parameter variation occurs additionally, caused by temperature effects, which influence the electrical as well as mechanical subsystem due to parameter dependencies of the piezoceramic layer, stator material, and contact layer.

III. IDENTIFICATION OF MODEL PARAMETERS

The control presented in Sections IV and V is based on the averaged model and parameterized by suitable identification methods. While parameters of the electrical and mechanical resonant tanks are estimated online (Section III-B), the parameters of the piezoelectric coupling matrix \mathbf{K}_{pv} and the values of C_p and R_{MRC} must be known in advance. In this section, a parameter identification method is presented based on investigations in the frequency domain.

A. Offline Identification of Piezoelectric Actuator Model

For parameter identification of the piezoelectric actuator model, its input and output quantities must be known. Since the electrical input signals (motor voltages \mathbf{v}_{cp} and currents \mathbf{i}_{Ls}) can only be measured, but not the output quantities of the piezoelectric actuator [acceleration \mathbf{a} (see Fig. 4)], the output quantities \mathbf{w} of the mechanical resonant system must be utilized. Therefore, the parameters of the piezoelectric actuator model can only be identified, when the mechanical subsystem is included [15]. Thus, the resonant frequency and the damping of the mechanical subsystem must be considered within the parameter identification, although these values are not of interest here. Since these parameters depend on the operation point (due to feedback forces \mathbf{F}_d ; see Section II-D), the identification task is impossible without additional measures. In order to deal with these nonlinearities, the rotor might be removed before performing the measurements. However, in this case, the mechanical vibration system and, therefore, the piezoelectric actuator is not loaded as compared to practical operation, because the inherent damping of the stator without the rotor is very low.

This disadvantage can be avoided when performing measurements with a constant bending wave in order to keep the parameters of the mechanical oscillation system constant. A constant

TABLE I
RESULTS OF THE PARAMETER IDENTIFICATION RELATED TO PIEZOELECTRIC COUPLING AND CROSS COUPLING

Bending wave's amplitudes \hat{w}	Estimated parameters			
	A_1 in N/V	A_2 in N/V	ϵ_1	ϵ_2
0.5 μm	0.532	0.294	0.196	0.020
0.6 μm	0.529	0.325	0.171	0.023
0.7 μm	0.515	0.350	0.163	0.023
0.8 μm	0.513	0.370	0.168	0.027
mean value	0.522	0.335	0.175	0.023
maximum deviation	0.010	0.041	0.021	0.004
	7.9% of 0.522		12% of 0.175	

bending wave is achieved using the control in Section IV, which is adjusted by provisional parameters in a first step.

Measured results are evaluated by a Simplex search method, varying arbitrary initialized parameters of the model in such a way that an appropriate loss function F is minimized. This loss function F is calculated from measured output signals \mathbf{w} and outputs \mathbf{w}' calculated by the model using the measured electrical input quantities

$$F = \sum_i [(w_{1s}^i + w_{1s}'^i)^2 + (w_{1c}^i + w_{1c}'^i)^2 + (w_{2s}^i + w_{2s}'^i)^2 + (w_{2c}^i + w_{2c}'^i)^2]. \quad (17)$$

During the experiment, the switching frequency ω_s is varied within a range of ± 400 Hz around the resonant frequency ω_m , while motor voltages \mathbf{v}_{cp} , currents \mathbf{i}_{Ls} , and modal amplitudes \mathbf{w} are measured every 50 Hz at frequencies ω_s^i (i measuring points). The parameter identification is performed for different amplitudes \hat{w} of the bending wave chosen to be 0.5 μm , 0.6 μm , 0.7 μm , and 0.8 μm and a temporal phase shift φ_m of 90° (perfect traveling wave; see Section V). Table I shows the results of parameter identification with respect to the piezoelectric coupling coefficients A_1 , A_2 and cross couplings ϵ_1 , ϵ_2 , while in Fig. 7, results for C_p and R_{MRC} are illustrated. In accordance with theory given in [15], variations of the amplitude \hat{w} result in small deviations of parameters A and ϵ only. However, in contrast to the results above, identification results of C_p and R_{MRC} show an increase of both parameters when the amplitude \hat{w} and, therefore, the amplitudes of currents \mathbf{i}_{Ls} are increased. This is affected by the hysteresis behavior of the piezoceramic, since the approximation by the linear equivalent electric circuit is only valid in a small operation range, as discussed in Section II. This motivates the need to perform the parameter identification in the operation range of interest, as mentioned above.

B. Online Identification of Resonance Parameters

With known parameters of the piezoelectric actuator, the input quantities $\mathbf{v}_i + \mathbf{v}_m$ of the electrical and \mathbf{a} of the mechanical subsystem can be calculated online. Since the USM drive is excited by sinusoidal signals at any time, it is possible to determine the parameters δ and ω_e of the resonant tanks by

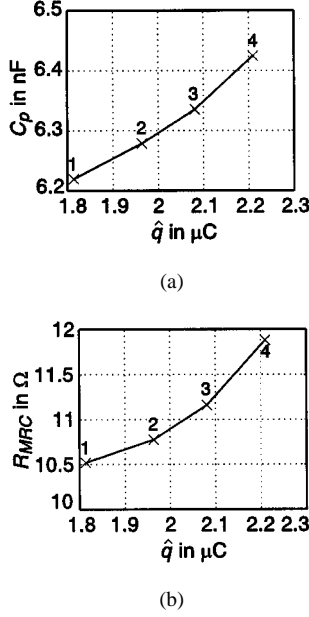


Fig. 7. Parameter identification of (a) C_p and (b) R_{MRC} at \hat{w} : 1: $0.5 \mu m$. 2: $0.6 \mu m$. 3: $0.7 \mu m$. 4: $0.8 \mu m$.

evaluation of its frequency responses at the operating point. The frequency response of resonant tanks is described by the static gain of transfer matrices \mathbf{G}_{el} and \mathbf{G}_m containing the damping coefficients δ and the frequency deviations $\Delta\omega = \omega_s - \omega_e$ of corresponding eigenvalues. Under consideration of steady-state operation mode and by applying appropriate simplifications, the following identification equations were derived in [11] for the electrical and mechanical subsystems:

$$\Delta\omega_{el} = -\omega_{el,P}^2 \frac{V_s V_{is} + V_c V_{ic}}{2\omega_s(V_s^2 + V_c^2)} \quad (18)$$

$$\delta_{el} = \omega_{el,P}^2 \frac{V_s V_{is} - V_c V_{ic}}{2\omega_s(V_s^2 + V_c^2)} \quad (18)$$

$$\Delta\omega_m = -\frac{W_s A_s + W_c A_c}{2\omega_s(W_s^2 + W_c^2)} \quad \delta_m = \frac{W_s A_s - W_c A_c}{2\omega_s(W_s^2 + W_c^2)} \quad (19)$$

$\omega_{el,P}$ (eigenfrequency at operating point) can be assumed as constant within the operating range. Since the impact of fast-changing parameter variations (caused by nonlinearities) will be compensated by measures explained in Section IV, only slow-varying characteristics (e.g., caused by temperature effects) must be identified. Thus, a pseudostationary evaluation of transfer functions can be performed by using low-pass filtering of the inputs and outputs of resonant tanks. Then, the complex identification task is reduced to simple algorithms.

IV. VOLTAGE AND BENDING WAVE CONTROL

In order to design a high-performance speed control, an appropriate torque adjustment is required. For this task, an inner bending wave control is indispensable, since the torque of the USM depends on the bending wave, as mentioned above. The proposed control scheme is depicted in Fig. 8. It is based on the averaged model outlined in Section II. Since the ultrasonic oscillations of the motor are characterized by cascaded electrical

and mechanical resonant systems, it is obvious to control the motor by means of an inner voltage and an outer bending wave control loop. Controlled quantities are the sine and cosine components of model voltages v_1, v_2 and modal amplitudes w_1, w_2 which are measured by phase-sensitive demodulation circuits in Fig. 2. In the following, the two-component controllers are designated as vector controllers. Since the USM is characterized by asymmetries between phases, nonideal motor properties can be compensated only, when an asymmetrical feeding by the motor voltages is applied (see Fig. 3). Thus, both phases must be controlled independently. Between the cascaded control structure and averaged model in Fig. 4(a), close coherence exists optimizing the drive control by the following systematic measures [11].

- The reference values v_i^* of the inverter stage are passed to the vector modulation algorithm in order to calculate the regulating quantities $\beta_1, \beta_2, \varphi_1$, and φ_2 . A compensation of mechanical feedback v_m on the converter is introduced. The voltage control is denoted by the vector controllers $\mathbf{G}_{Rel1,2}$.
- A compensation of piezoelectric couplings between the vibration modes is achieved by introducing the inverse model of the piezoelectric actuator

$$v^* = K_{pv}^{-1}(a^* + a_w). \quad (20)$$

- By this measure, both phases can be controlled independently and, therefore, an identical vector control scheme can be applied for the bending wave control $\mathbf{G}_{Rm1,2}$ as used for the voltage control. The command inputs of bending wave control are the amplitude \hat{w}^* of traveling bending wave and the phase φ_m^* between both standing waves. These reference values are obtained from the speed control and are transformed from polar to Cartesian coordinates, as explained in Section V.
- Remaining regulating quantity ω_s of the converter is tracked in such a way that the vibration modes of the stator are excited at resonance by means of $\Delta\omega_m^* = 0$ (see Sections IV-B and IV-D).
- Utilizing the power performance of the drive control for wide-range operations with respect to high dynamic responses, an online adaptation of control parameters and a disturbance compensation are recommended due to nonlinear contact impacts and temperature influences (see Section IV-B).

A. Vector Control Scheme for Resonant Structures

The state variables v and w of resonant tanks are controlled by vector controllers \mathbf{G}_R , which are identical in structure for the electrical and mechanical oscillation systems. Designing \mathbf{G}_R transfer matrices \mathbf{G}_{el} of electrical plant (5) and \mathbf{G}_m of mechanical plant (13) must be considered, which are characterized by transfer functions G_C describing dynamical cross couplings between the Cartesian input and output quantities. In order to reduce the control design of one resonant system to a single-loop control for each Cartesian quantity, a decoupling structure is required. The decoupling of resonant structure \mathbf{G} (describing \mathbf{G}_{el}

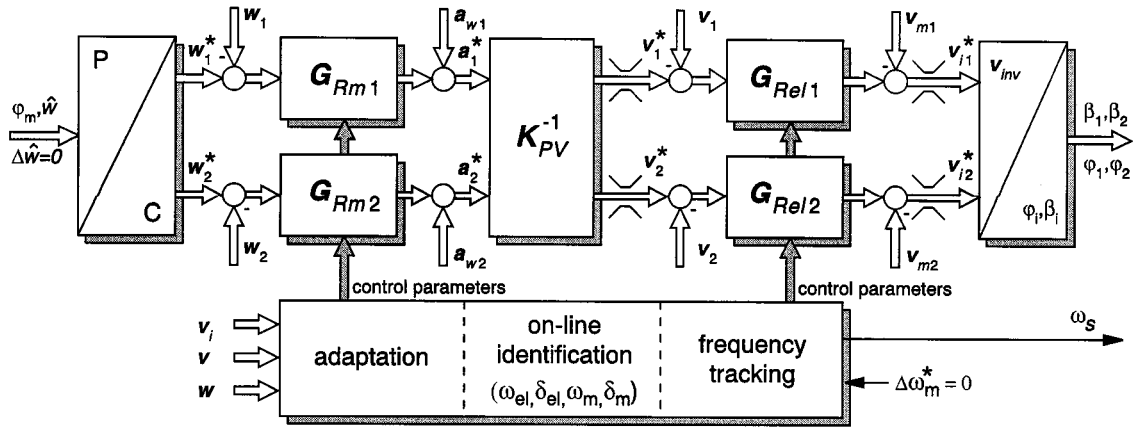


Fig. 8. Voltage and bending wave vector control scheme.

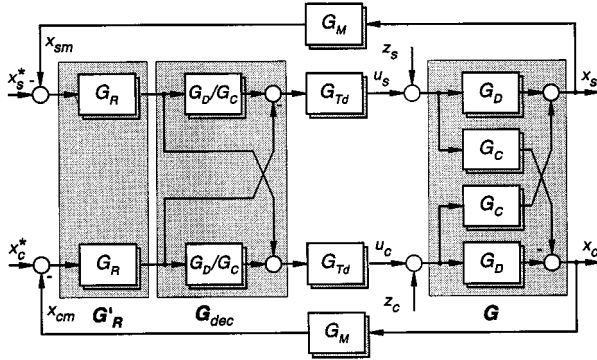


Fig. 9. Vector control scheme for resonant structure.

and G_m) is achieved when decoupling matrix G_{dec} is introduced between plant and control by

$$\begin{aligned} G \cdot G_{dec} &= \begin{bmatrix} G_D & G_C \\ -G_C & G_D \end{bmatrix} \begin{bmatrix} G_D/G_C & -1 \\ 1 & G_D/G_C \end{bmatrix} \\ &= \frac{G_D^2 + G_C^2}{G_C} \begin{bmatrix} 1 & 0 \\ 0 & 1 \end{bmatrix}. \end{aligned} \quad (21)$$

This decoupling measure guarantees an operation at mechanical resonance, which is one important goal of the control. As investigated in [11], the decoupled plant $(G_D^2 + G_C^2)/G_C$ can be well approximated by a first-order lag containing damping coefficient δ as time constant and frequency deviation $\Delta\omega$ as dominant static gain. Besides these dynamics, the behavior of the underlaid systems (denoted by G_{Td}) and the measuring systems G_M must be taken into account for the design of the vector control in Fig. 9. While underlaid systems of the voltage control are given by deadtimes of the digital control and modulator, the underlaid system of the bending wave control is given by the closed-loop voltage control. For the single-loop controllers G_R , proportional-integral (PI) controllers are designed in [11], applying an analytical design method called "digital amount optimum." An analytical synthesis method is privileged due to the aimed application of an online adaptation of vector controllers.

In order to verify the vector control scheme for resonant structures, the converter is loaded by a capacitance C_P and resistance R_{MRC} , which are equivalent to motor parameters for typical operation. Fig. 10 illustrates a comparison between results obtained by simulation and measurement in case of a step-like command and disturbance change. As is seen, first, a good agreement between simulation and experiment is obtained, second, the decoupling structure works fine, and third, the design method offers acceptable dynamic responses.

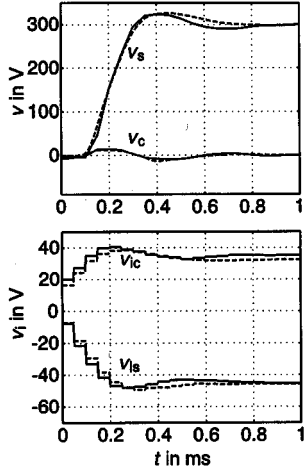
B. Compensation of Nonlinearities and Temperature Effects

Results so far consider only linear time-invariant motor characteristics. When applying the cascaded vector control scheme for the drive control, appropriate measures for compensation of nonlinear feedback forces and temperature effects must be developed.

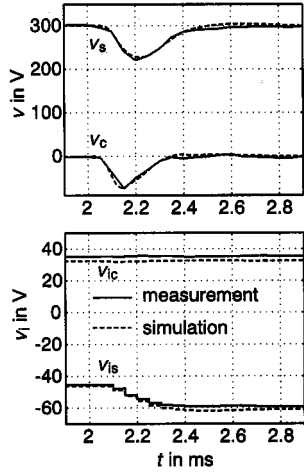
In Section II, a linearized model (16) of the vibrating system is derived. In order to meet the assumption for linearization, first, the controllers have to be adapted, and second, the disturbances by $\Delta\delta_m$, $\Delta\tilde{\omega}_m$ and $\Delta\omega_s$ must be eliminated. Temperature effects are compensated by adaptation of controllers using parameters obtained by the online identification in Section III. Additionally, the fast-changing disturbances can be suppressed when using the remaining, regulating quantity ω_s of the converter. By introducing a fast frequency precontrol $\Delta\omega_{s,f}$, the frequency is modulated in such a way that the dominant disturbance of the fast-varying eigenfrequency shift in (16) [described by $\Delta\omega_m(\hat{w})$] is compensated through

$$\begin{aligned} \Delta\omega_{s,f} &= \Delta\tilde{\omega}_m(\hat{w}) \quad \text{with} \\ \hat{w} &= \sqrt{(w_{1s}^2 + w_{1c}^2 + w_{2s}^2 + w_{2c}^2)/2}. \end{aligned} \quad (22)$$

By this measure, the disturbance $\Delta\tilde{\omega}_m$ of the linearized model (16) is eliminated together with achieving a fast adaptation of the control, since the frequency deviation $\Delta\omega_m$, which has an impact on the dynamics of transfer matrix G_m , is always constant. By investigation, it turned out that the characteristic $\Delta\tilde{\omega}_m(\hat{w}) = f(\hat{w})$ can be well approximated by a linear relation within the operating range of \hat{w} . Due to smaller influences of



(a)



(b)

Fig. 10. (a) Command response of voltage control by $v_s^* = 300$ V at $t = 0$. (b) Disturbance response caused by $z_s = 15$ V at $t = 2$ ms.

$\Delta\delta_m$, its impact is neglected and must be compensated by the robustness of the control.

As introduced above, the mechanical subsystem is excited at resonance for optimized operation mode (Section IV-D). This requirement is satisfied when applying a slow frequency tracking in addition to the fast frequency precontrol. A correct stationary tracking of resonance frequency is achieved when establishing a control unit by

$$\Delta\bar{\omega}_m = (\Delta\omega_{m1} + \Delta\omega_{m2})/2 \equiv 0 \quad (23)$$

using parameters identified by (19).

The total scheme of online identification, adaptation, and frequency modulation is depicted in Fig. 11. By implementing an I-controller for the slow frequency tracking, the requirement in (23) is guaranteed (ω_{s0} initial value). Under common consideration of the combined structure of the I-controller and online identification, the frequency tracking represents a first-order lag and not a closed-loop frequency control.

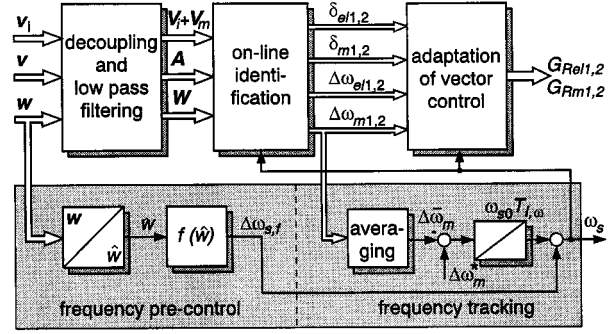
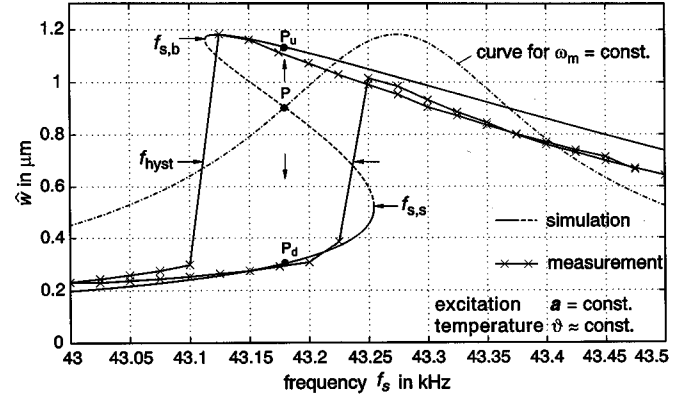
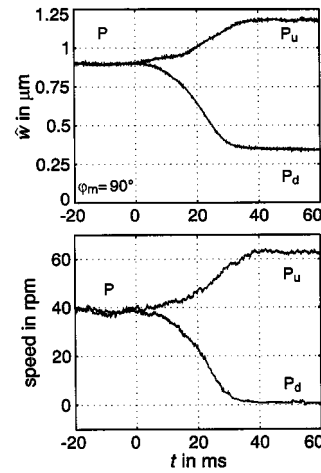


Fig. 11. Online identification, adaptation, and frequency modulation.



(a)



(b)

Fig. 12. (a) Nonlinear frequency characteristics of mechanical subsystem. (b) Instability caused by turn-off of bending wave control at $t = 0$.

C. Pull-Out Phenomenon and Hysteresis Effect

Nonlinear contact impact causes stability problems with respect to the frequency response, since the well-known pull-out phenomenon of traveling-wave USM's occurs, as observed in [2], [4]. As illustrated in Fig. 12(a), this breakdown ($f_{s,b}$) appears when the feeding frequency ω_s is decreased below the resonance frequency ω_m . By increasing ω_s until the actual resonance frequency is attained again ($f_{s,s}$), the rotor starts

to revolve abruptly. Since a hysteresis loop is obtained when changing ω_s in this way, the effect is designated as hysteresis effect.

The reason is related to a degressive stiffness behavior of the contact mechanism, since variations of the amplitude \hat{w} influence the resonance frequency ω_m , as mentioned above. For investigation of the nonlinear frequency characteristics of mechanical resonant tanks, the gain is calculated by

$$|\hat{w}/a| = 1 / \sqrt{(\omega_{0m}^2(\hat{w}) - \omega_s^2)^2 + 4\delta_m^2\omega_s^2} \quad (24)$$

using the contact model in [8]. In Fig. 12(a), the calculated results are compared with measurements. While outside the hysteresis bandwidth single-valued curves are obtained, inside the bandwidth three solutions are calculated. Two of them are stable operating points, indicated also by the measured curve. It can be shown that operating points marked by the dashed line characterize instabilities in the case of frequency control, which must be taken into account when designing the drive control.

Previously published control schemes always use frequency modulation for controlling the amplitude \hat{w} . It is obvious that the pull-out phenomenon can be avoided only when a certain distance between resonance frequency ω_m and switching frequency ω_s is introduced (e.g., see [4]), consequently losing a wide range of the performance of the USM, which is discussed in Section IV-D. Since amplitude modulation is applied in Fig. 8 instead of frequency modulation for controlling \hat{w} , operating points indicated as instabilities in Fig. 12(a) can be stabilized. Thus, the pull-out phenomenon can be suppressed in general offering an additional degree of freedom for frequency tracking.

In Fig. 12(b), the effect of stabilization is examined for operating points which are unstable in the case of frequency control. The reference value of the controlled amplitude is chosen to be $\hat{w}^* = 0.9 \mu\text{m}$ and the difference $\Delta\omega_m$ is about $-2\pi \cdot 50 \text{ Hz}$, which characterizes the operating point P in Fig. 12(a). At time $t = 0 \text{ ms}$, the bending wave control is turned off. Due to small disturbances, in practice, the operating point of the voltage controlled drive shifts from unstable point P to stable point P_u or P_d (high speed or standstill). Operating points P_u or P_d belong to the hysteresis curve in Fig. 12(a). As shown by these measurements, operation of USM drives at the mechanical resonance and below this critical point is possible when using a suitable drive control.

D. Experimental Results of Bending Wave Control

When operating the drive at the mechanical resonance frequency, the optimal operating point of the vibrator is found minimizing the voltage demand for excitation, reducing losses of the converter and piezoelectric ceramic (see Fig. 14). In order to prove the voltage decrease, measurements for different deviations $\Delta\omega_m$ between ω_s and eigenfrequencies ω_m within an appropriate range of the feeding frequency are performed and depicted in Fig. 13. Since the bending wave is kept constant by the control, eigenfrequencies ω_m can be assumed as constant, too, and the voltage curves characterize the inverse behavior of linear mechanical resonant circuits. A remarkable reduction of the voltage demand of the USM is achieved in contrast to previously published control schemes, which keep a certain fre-

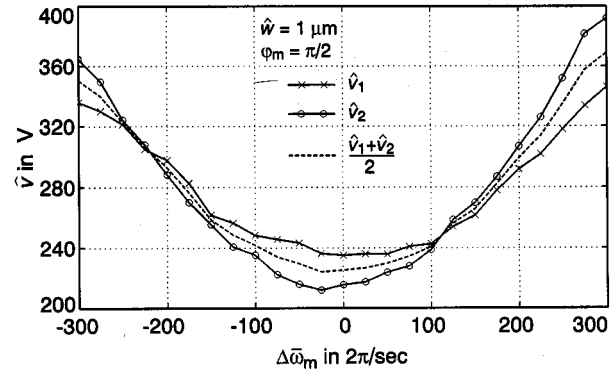


Fig. 13. Voltage requirement versus $\Delta\omega_m$ for constant modal amplitudes.

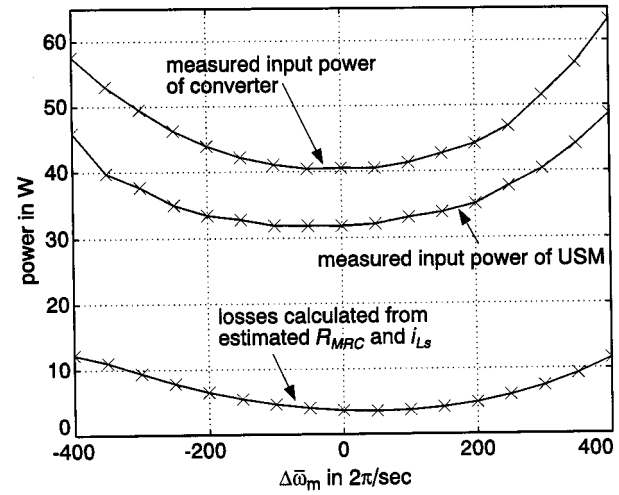


Fig. 14. Power distribution of USM drive.

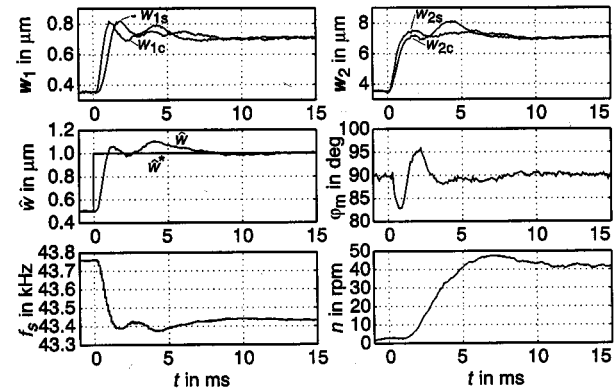


Fig. 15. Large signal response of bending wave control for step change of \hat{w} .

quency distance $\Delta\omega_m$ to ω_m of several hundred hertz to avoid the pull-out phenomenon.

In Fig. 14, the power losses within the USM drive are shown. In particular, losses affected by R_{MRC} (see Section II-B) can be minimized when operating the USM at resonance, as mentioned above.

In Fig. 15, measured results of a transient response are depicted. A large step-like command of the amplitude from $\hat{w}^* = 0.5 \mu\text{m}$ to $\hat{w}^* = 1 \mu\text{m}$ [$|w_{s,c}| = 353 \text{ nm}$ to $|w_{s,c}| = 707 \text{ nm}$;

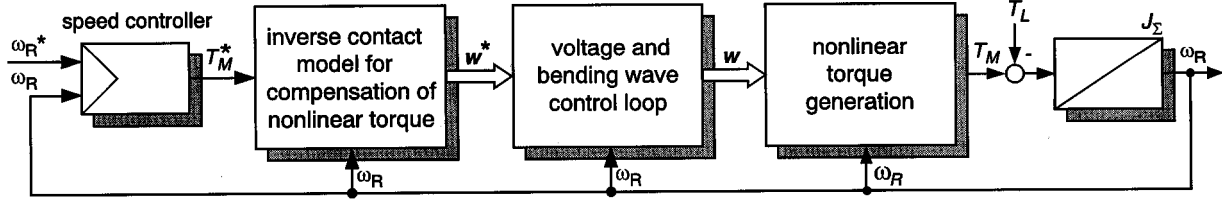


Fig. 16. Speed and torque control scheme.

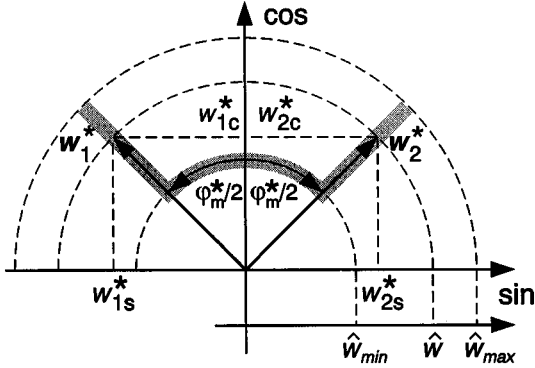


Fig. 17. Set-point adjustment for optimized force transmission.

see (25)] at $t = 0$ ms is performed. The phase and frequency deviations are kept constant to $\varphi_m^* = 90^\circ$ and $\Delta\omega_m^* = 0$.

As indicated by the measurements, the rise time of the modal amplitudes is only about 1 ms, and note that the decoupling works sufficiently. By the fast frequency precontrol, a large shift of f_s of about $2\pi \cdot 400$ Hz is modulated, tracking the eigenfrequencies ω_m during the transient reaction of the amplitude \hat{w} . In comparison with the results in Fig. 10, deviations occur due to the neglected impacts of disturbance $\Delta\delta_m$. However, a step-like command of such a large amount is not applied by the speed control. Thus, the measured response satisfies requirements of the outer control loops.

V. TORQUE AND SPEED CONTROL

While the torque of conventional electromagnetic motors is dependent almost linearly on the current of the motor, the torque T_M of USM's is dependent nonlinearly on the amplitudes \hat{w}_1, \hat{w}_2 of both standing waves, the temporal phase shift φ_m , and the rotor's speed ω_R , (e.g., see [9]). For realizing a high-performance speed control, the concept shown in Fig. 16 is proposed, based on the compensation of the nonlinear torque generation of the USM by its inverse characteristic, called the inverse contact model.

This concept yields two important advantages.

- On the one hand, open-loop torque control is enabled.
- On the other hand, a speed control loop can be realized by applying a linear speed controller, which is well known from conventional electrical drives with linear loads.

A. Set-Point Adjustment for Torque Control

Since there is more than one degree of freedom for adjusting the speed–torque characteristic by the bending wave, an appro-

prate set-point adjustment must be chosen. In [12], it is pointed out that an operation with a perfect traveling wave goes along with minimized losses caused by the friction mechanism. These conditions are obtained when amplitudes \hat{w}_1, \hat{w}_2 are equal to a single value \hat{w} and phase φ_m is kept to $\pm 90^\circ$. Thus, variations of speed–torque curves should be performed by adjusting \hat{w} first. Second, it is considered that amplitude \hat{w} cannot be decreased under a certain threshold \hat{w}_{\min} due to stick effects at low amplitude which cause a sudden stop of the rotor rotation. Operating the drive in this inherent dead zone, a nonperfect traveling wave is required by adjusting phase φ_m and controlling the amplitude above the threshold. Therefore, a set-point adjustment is chosen which guarantees minimized losses within a wide operation range, but continuous behavior within the whole operation range, as illustrated in Fig. 17.

- In any operation mode, the amplitudes of both standing waves are equal, established by $\Delta\hat{w}^* = \hat{w}_1^* - \hat{w}_2^* = 0$.
- In the high-speed/high-torque region, the USM is operated with a perfect traveling wave, obtained by adjusting $\hat{w}_{\min} \leq \hat{w} \leq \hat{w}_{\max}$ and $|\varphi_m| = 90^\circ$.
- In the low-speed/low-torque region, the phase shift φ_m is used for the control and the amplitude is kept to its threshold $\hat{w} = \hat{w}_{\min}$.

The Cartesian reference values of the bending wave control scheme are calculated by

$$\begin{aligned} w_{1s}^* &= -\hat{w}^* \sin(\varphi_m^*/2) \\ w_{1c}^* &= \hat{w}^* \cos(\varphi_m^*/2) \\ w_{2s}^* &= \hat{w}^* \sin(\varphi_m^*/2) \\ w_{2c}^* &= \hat{w}^* \cos(\varphi_m^*/2). \end{aligned} \quad (25)$$

Under consideration of the statements given above, measured curves of the USM under study are depicted in Fig. 18. While in the high-speed/high-torque range the amplitude is varied from $\hat{w}_{\min} = 0.7 \mu\text{m}$ to $\hat{w}_{\max} = 1.2 \mu\text{m}$ in steps of $0.1 \mu\text{m}$ (solid lines), in the low-speed/low-torque region, the phase φ_m is adjusted to $[-50^\circ, -30^\circ, -15^\circ, 0^\circ, 15^\circ, 30^\circ, 50^\circ]$ (dashed lines) controlling the amplitude above the threshold for continuous operation. Torque and speed of the USM are limited to $|T_M| = 3 \text{ N}\cdot\text{m}$ and $|n| = 80 \text{ r/min}$ to prevent destruction.

B. Inverse Contact Model by Neural Network

Since analytical contact models describing the nonlinear torque generation are not sufficiently accurate, and are complicated, a numerical approach based on measurements (see Fig. 18) is predestined for realizing the inverse contact model.

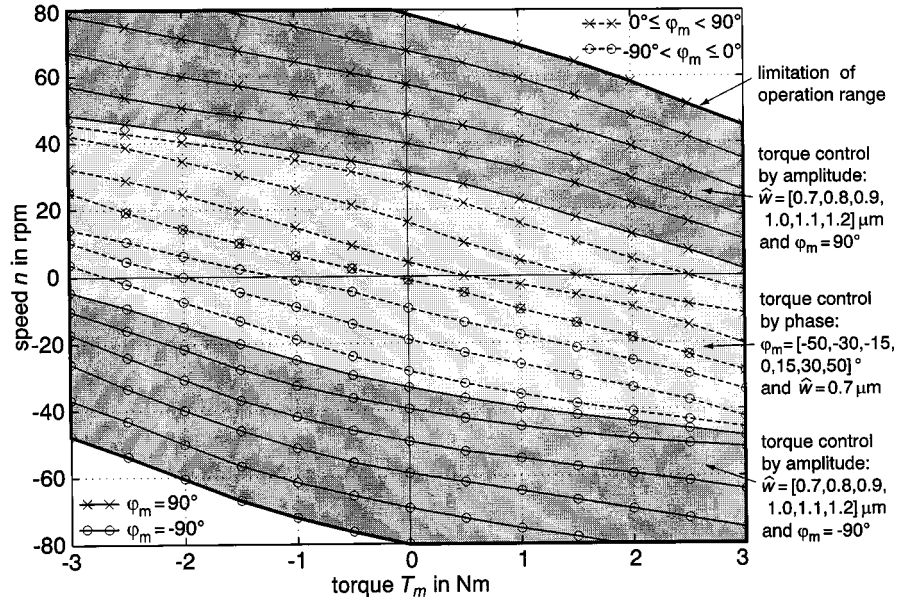


Fig. 18. Measured speed-torque curves.

For this task, a basis function network (BFN) is proposed for describing the inverse speed-torque characteristic.

In order to generate the reference values of the bending wave control from desired torque T_M^* under consideration of actual motor speed ω_R , a two-dimensional BFN with linear splines is implemented for the inverse contact model which is trained offline by the sample points of Fig. 18. It serves for interpolation between the samples of a lookup table.

Since regulating quantities \hat{w}^* , φ_m^* are not varied independently (by this approach, only one quantity is varied at the same time), it is possible to represent the set-point adjustment by one scalar and normalized regulating quantity w_n when introducing the transformation defined in

$$w_n = \begin{cases} \frac{1 - w_{n\alpha}}{\hat{w}_{\max} - \hat{w}_{\min}} (\hat{w} - \hat{w}_{\max}) + w_{n\alpha}, & \text{for } \hat{w}_{\min} \leq \hat{w} \leq \hat{w}_{\max}, \varphi_m = 90^\circ \\ w_{n\alpha} \cdot \sin(\varphi_m), & \text{for } \hat{w} = \hat{w}_{\min}, -90^\circ < \varphi_m < 90^\circ \\ \frac{w_{n\alpha} - 1}{\hat{w}_{\max} - \hat{w}_{\min}} (\hat{w} - \hat{w}_{\min}) - w_{n\alpha}, & \text{for } \hat{w}_{\min} \leq \hat{w} \leq \hat{w}_{\max}, \varphi_m = -90^\circ. \end{cases} \quad (26)$$

Thus, one BFN is sufficient for modeling the inverse characteristics and output quantity w_n represents the actual regulating quantity either for operations in the high-speed/high-torque or low-speed/low-torque regions. Using (26), the net should be designed by:

- 1) nonlinear transformation $\sin(\varphi_m)$, satisfying an even distribution within the low-speed/low-torque range, since the no-load speed is roughly proportional to $\sin(\varphi_m)$ (see Fig. 18);
- 2) transparent parameter $w_{n\alpha}$, which represents the boundary value between the two different operation

modes and is introduced for scaling them in order to achieve an almost even slope of approximated inverse model within the common neural net for w_n ;

- 3) deviation between training (reference) data $w_{n,ref}$ and net output w_n denoted by $\Delta w_n = w_{n,ref} - w_n$ and the size of neural layer, requiring a compromise between accuracy and the amount of neurons.

The BFN designed for the inverse contact model consists of 41×13 neurons for the speed and torque input. Parameter $w_{n\alpha}$ is set to 0.4. After learning, a final fault Δw_n of less than 3% within the whole input ranges is obtained. This accuracy is required because of the large dependence on torque versus speed (see Fig. 18). An appropriate training algorithm is explained in [12].

However, the BFN represents the inverse speed-torque characteristic with output quantity w_n depicted in Fig. 19. The limitation of the bending wave's amplitude by \hat{w}_{\max} is considered by $|w_n| \leq 1$. For generating the regulating quantities \hat{w}^* and φ_m^* , the inverse transformation of (26) is performed.

C. Speed Control Scheme

Since the reference values of the bending wave control are calculated from the desired torque value T_M^* by the BFN under consideration of actual motor speed ω_R , the remaining nonlinearity is compensated and an almost linear relation between reference torque T_M^* and motor torque T_M is obtained. Thus, the command behavior of the new actuator approaches that of conventional electrical drives and is, thus, attractive for applications in the field of servo systems. Proven schemes can be applied when designing the speed control depending on the application, as illustrated in Fig. 16. Since the mechanical load of the test setup can be described by a one-mass system, a PI speed controller is the proper choice for the application.

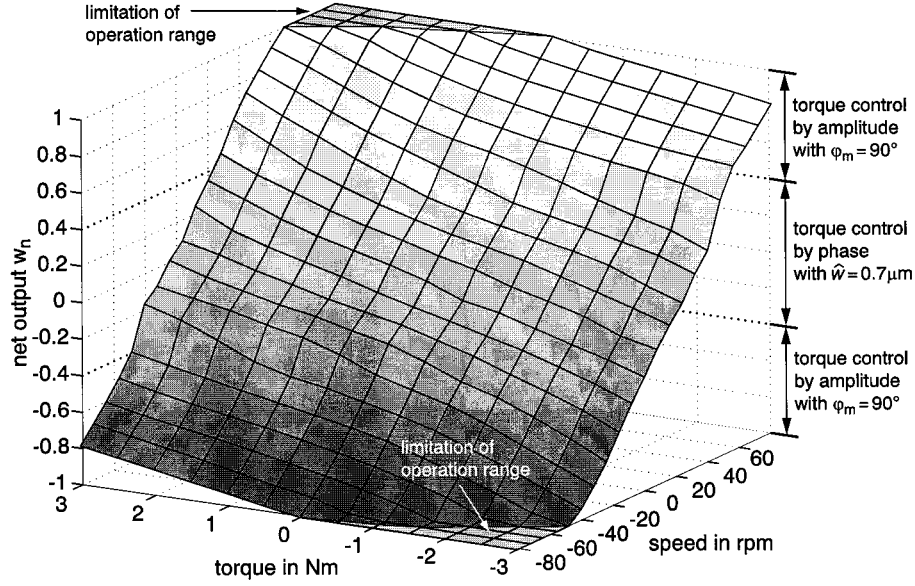


Fig. 19. Inverse speed–torque characteristic with w_n as output quantity.

D. Experimental Results of Speed Control

In Fig. 20, the measured transient responses of the speed control are shown, while in Fig. 21, the operation is illustrated by the corresponding speed–torque trajectories within the operating range of Fig. 18.

In case (a), a step-like command from the low-speed/low-torque region (operating point $P1$ with $n = 10$ r/min and $T_L = 0$) into the high-speed/high-torque region (operating point $P2$ with $n = 50$ r/min and $T_L = 0$) is performed. During the first time interval $0 \leq t \leq 3$ ms, the reference value of phase φ_m is increased by the BFN due to reference torque T_M^* , while the reference value of the amplitude is kept to $\hat{w}_{\min} = 0.7 \mu\text{m}$. When φ_m^* attains 90° at $w_n = w_{n\alpha} = 0.4$, the speed is regulated by varying the reference value of the wave's amplitude \hat{w} , operating the drive with a perfect traveling wave. After a short rise time of about 10 ms, the desired speed is attained and the drive's speed n settles smoothly on $n^* = 50$ r/min. Since the USM drive is accelerated during this response, the speed–torque trajectory for case (a) passes almost the first (motory) quadrant in Fig. 21.

Case (b) depicts the inverse operation: $P2 \rightarrow P1$. Due to the sufficient compensation of nonlinear torque generation by the BFN, the response time, overshoot, and shape of the curve is approximately identical when compared to case (a). Since the drive is decelerated in case (b), the corresponding speed–torque trajectory passes almost the second (nonmotory) quadrant in Fig. 21.

Case (c) shows a speed reversal of the drive. During interval $0 \leq t \leq 2$ ms, the reference torque T_M^* is increased to its boundary value of 3 N·m. After its boundary value is attained, a linear deceleration of the drive's speed toward $n = 0$ appears due to the constant motor torque. At time $t = 7$ ms, the reference torque is decreased below its boundary and the speed control works finally in a linear operation mode, accelerating the drive toward $n^* = 50$ r/min. In the intermediate interval, the

controlled phase is varied smoothly from its negative to its positive maximum.

In case (d), the disturbance behavior is investigated performing a step-like load change from zero to $T_L = 1$ N·m: $P4 \rightarrow P5$. Due to the relative small inertia of the drive system, the speed is affected largely by the load disturbance, but corrected within 30 ms to its reference value of $n^* = -40$ r/min.

As indicated by elaborated measurements, first, the designed torque and speed control scheme ensures the optimized conditions as outlined by the speed–torque characteristics in Fig. 18 for high-speed/high-torque and low-speed/low-torque operation. Second, the inverse contact model by the BFN, applied for compensation of nonlinear torque generation, operates satisfactory as indicated by the expected transient responses of the speed control.

VI. USM DRIVE APPLIED TO AN ACTIVE CONTROL STICK (ACS)

Finally, an ACS realized by means of the torque- and speed-controlled USM drive is noted as an interesting kind of application. One main disadvantage of the conventional side stick, realizing the “fly-by-wire” concept in modern aircrafts, is the absence of any feedback from the rudders. In order to reproduce feedback forces artificially (called active force feedback and outlined in Fig. 22), an actuator has to be introduced in the mechanical assembly of the stick. By the ACS, it is also possible to generate an adjustable reset force, to couple the pilot's and copilot's sticks by wire and to produce stick vibrations as a mechanical warning signal for the pilot. Due to their high power density and high torque at low rotational speed, piezoelectric motors seem to be advantageous for this application. In cooperation with DaimlerChrysler AG and SFIM-Industries, a uniaxial prototype ACS (see Fig. 23) [13] was successfully realized by

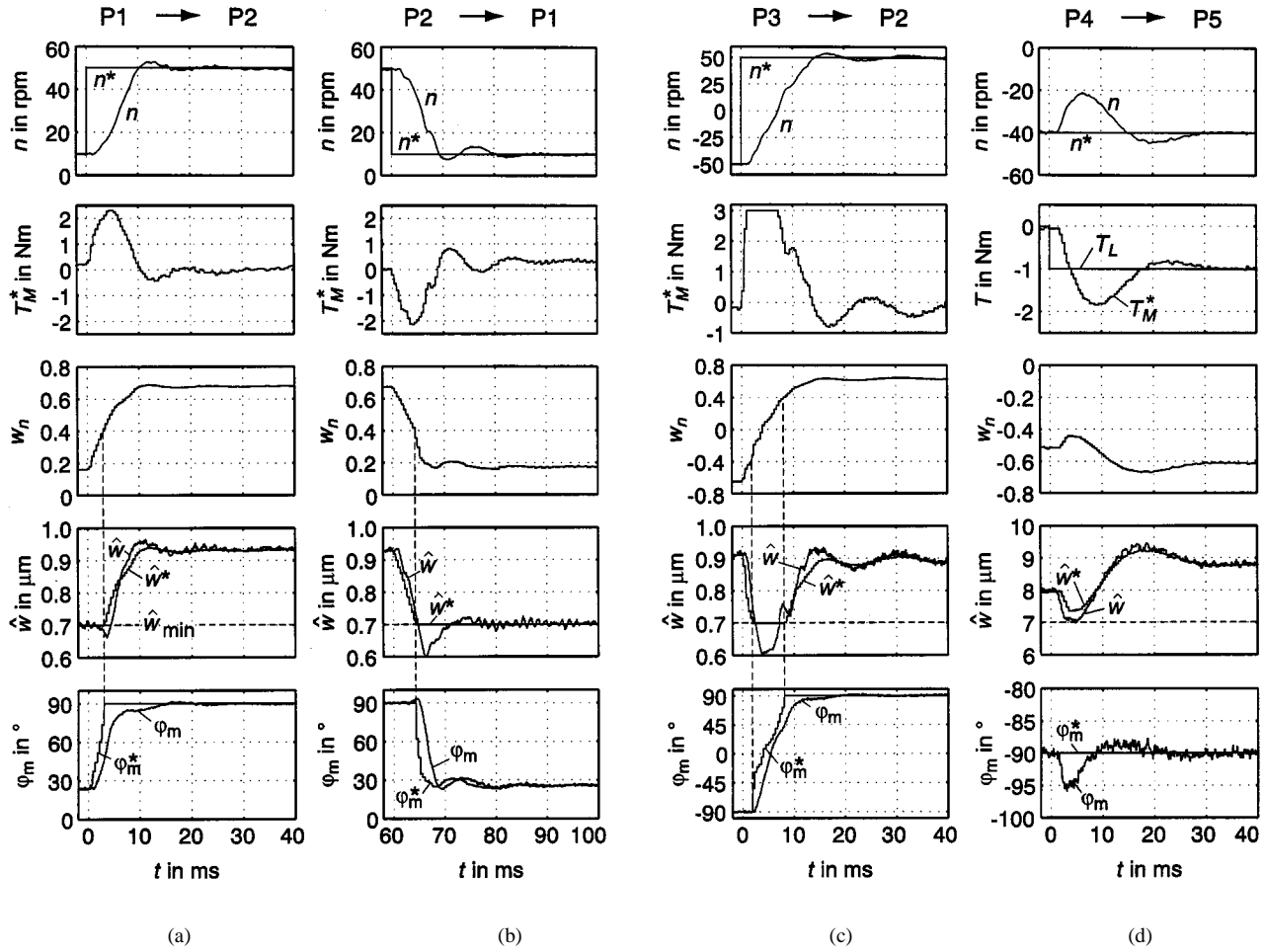


Fig. 20. Experimental results of speed control.

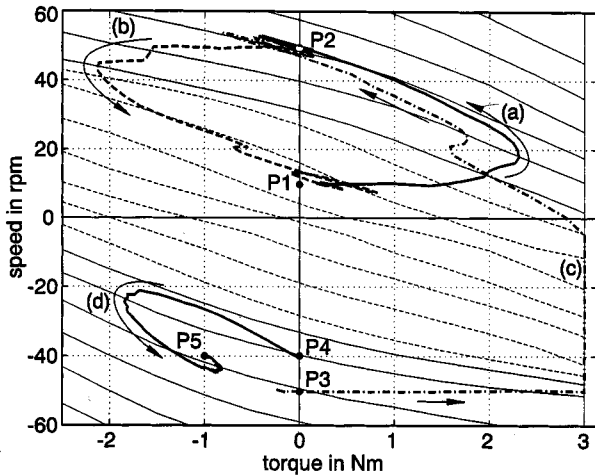


Fig. 21. Speed-torque trajectories of Fig. 20 within speed-torque region of Fig. 18.

the USM drive using controls developed in the previous sections.

The control scheme for the ACS reproduces the reset force represented by a nonlinear spring characteristic and superimposes feedback torque T_{FB} . Since no torque measurement

system is applied for the prototype ACS, it is realized by open-loop torque control using the inverse contact model.

For this task, the speed control in Fig. 16 is extended by an additional outer position control loop and the reference value (desired position α_S^* of the stick) is generated by the inverse relation of the nonlinear reset characteristic (see Fig. 22). As the input signal for the inverse relation, the reference torque T_M^* is used (operation without torque measurement system) regulating the ACS in such a way that the nonlinear reset characteristic is reproduced as desired when torque T_S resulting from pilot's force F_P is applied to the stick. Feedback can be superimposed easily by T_{FB} , as illustrated in Fig. 22. The control system reacts stably in any way and necessary limitations of speed and torque can be realized easily by limitation of their reference values.

Fig. 24 shows measured torque curves T_S versus stick position α_S of the realized uniaxial ACS in comparison with the desired torque T_M^* given by the nonlinear reset characteristic. The operation range of interest is passed through by constant speed ($T_S = T_M$; steady-state operation) in both directions (increase of stick position and decrease of stick position). The deviations are about 15% of the maximum torque value, which represents inaccuracies of the inverse contact model (open-loop torque control) mainly affected by the neglected temperature effects on the torque generation. However, these deviations cannot

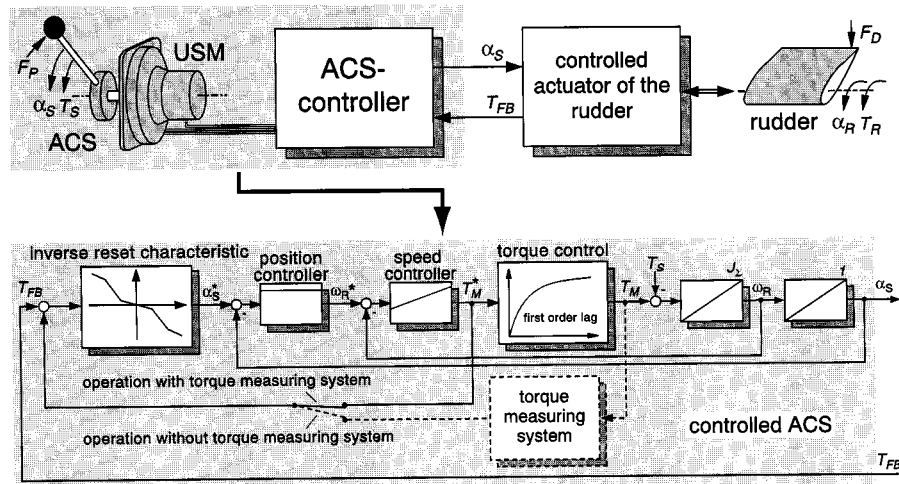


Fig. 22. Control scheme for ACS.

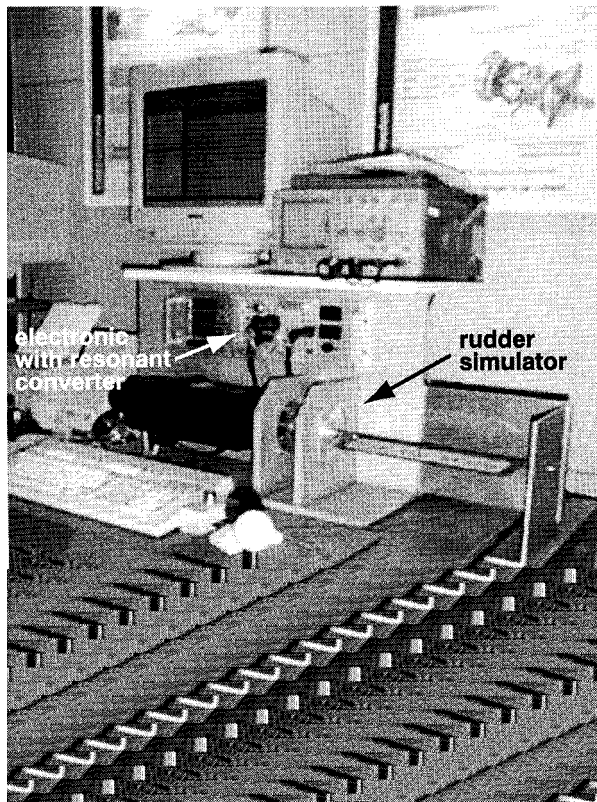


Fig. 23. Prototype ACS and test setup.

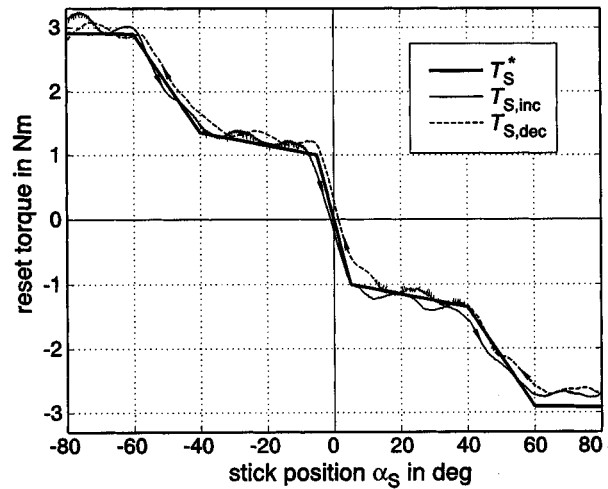


Fig. 24. Nonlinear reset characteristic reproduced by the ACS.

VII. CONCLUSION

be sensed by the pilot. In practice, the accuracy can be increased by a torque measurement system, as illustrated by the dashed block and signal line in Fig. 22. In this case, open-loop torque control means an alternative operation mode or, rather, a possibility for monitoring the system and, therefore, an increase in safety. The designed ACS control turns out to be a suitable measure for this kind of application. The proposed concept of the ACS and active force feedback is also interesting for other kinds of "by-wire" application.

This paper has proposed a novel control scheme for traveling-wave-type USM's. In order to obtain high performance, a systematic design approach by a motor model is applied using the inverse model structure for the cascaded control. Since all dominant nonlinearities are taken into account, an attractive dynamic behavior and a remarkable reduction of losses are achieved. By outer control loops for torque and speed, compensating the nonlinear speed-torque characteristic, first, the command behavior approaches that of conventional electrical drives, and second, losses caused by the friction mechanism are minimized. The outer controls are based on inner control loops for the electrical and mechanical oscillation systems. The nonlinear and time-variable behavior of the oscillation systems is almost compensated by online identification of parameters, adaptation of controllers, and frequency tracking. By these measures, operation at the mechanical resonance is enabled, minimizing the losses of the electrical subsystem remarkably. The potential of

optimization with respect to dynamics and efficiency is demonstrated by experimental results, and the applicability of the drive control to servo systems is pointed out by an ACS realized by a USM.

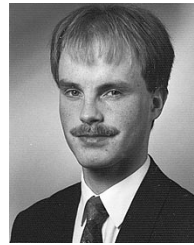
REFERENCES

- [1] T. Sashida and T. Kenjo, *An Introduction to Ultrasonic Motors*. Oxford, U.K.: Clarendon, 1993.
- [2] S. Furuya, T. Maruhashi, Y. Izuno, and M. Nakaoka, "Load-adaptive frequency tracking control implementation of two-phase resonant inverter for ultrasonic motor," *IEEE Trans. Power Electron.*, vol. 7, pp. 542–550, July 1992.
- [3] N. Hagood and J. McFarland, "Modeling of a piezoelectric rotary ultrasonic motor," *IEEE Trans. Ultrason., Ferroelect., Freq. Contr.*, vol. 42, pp. 210–224, Mar. 1995.
- [4] T. Senjyu, H. Miyazato, S. Yokoda, and K. Uezato, "Speed control of ultrasonic motors using neural network," *IEEE Trans. Power Electron.*, vol. 13, pp. 381–387, May 1998.
- [5] F.-J. Lin, "Fuzzy adaptive model-following position control for ultrasonic motor," *IEEE Trans. Power Electron.*, vol. 12, pp. 261–268, Mar. 1997.
- [6] M. Goldfarb and N. Celanovic, "Modeling piezoelectric stack actuators for control of micromanipulation," *IEEE Contr. Syst. Mag.*, vol. 17, pp. 69–79, June 1997.
- [7] J. Maas, P. Krafka, N. Fröhleke, and H. Grotstollen, "Prototype drive and modulation concepts for DSP-controlled ultrasonic-motors powered by resonant converters," in *Proc. 6th European Conf. Power Electronics and Applications*, vol. 1, Seville, Spain, Sept. 1995, pp. 1777–1782.
- [8] J. Maas, P. Ide, N. Fröhleke, and H. Grotstollen, "Simulation model for ultrasonic motors powered by resonant converters," in *Conf. Rec. IEEE-IAS Annu. Meeting*, vol. 1, Lake Buena Vista, FL, Oct. 1995, pp. 111–120.
- [9] J. Maas, P. Ide, and H. Grotstollen, "Characteristics of inverter-fed ultrasonic motors—Optimization of stator/rotor-interface," in *Proc. 5th Int. Conf. New Actuators*, Bremen, Germany, June 1996, pp. 241–244.
- [10] J. Maas and H. Grotstollen, "Averaging model for inverter-fed ultrasonic motors," in *Proc. IEEE PESC'97*, vol. 1, St. Louis, MO, June 1997, pp. 740–746.
- [11] J. Maas, T. Schulte, and H. Grotstollen, "Optimized drive control for inverter-fed ultrasonic motors," in *Conf. Rec. IEEE-IAS Annu. Meeting*, vol. 1, New Orleans, LA, Oct. 1997, pp. 690–698.
- [12] —, "Controlled ultrasonic motor for servo-drive applications," in *Proc. 4th Europ. Conf. Smart Structures and Materials—2nd Int. Conf. Micromechanics, Intelligent Materials and Robotics*, Harrogate, U.K., July 1998, pp. 701–708.
- [13] T. Schulte, H. Grotstollen, H.-P. Schöner, and J.-T. Audren, "Active control stick driven by a piezoelectric motor," in *Proc. 3rd Int. Symp. Advanced Electromechanical Motion Sys.*, vol. 1, Patras, Greece, July 1999, pp. 583–588.
- [14] J. Maas and T. Schulte, "High performance speed control for ultrasonic motors," in *Proc. IEEE/ASME Int. Conf. Advanced Intelligent Mechatronics*, vol. 1, Atlanta, GA, Sept. 1999, pp. 91–96.
- [15] T. Schulte and N. Fröhleke, "Parameter identification of ultrasonic motors," in *Proc. IEEE/ASME Int. Conf. Advanced Intelligent Mechatronics*, vol. 1, Atlanta, GA, Sept. 1999, pp. 97–102.



Jürgen Maas was born in Nieheim, Germany, in 1965. He received the Dipl.-Ing. and Ph. D. degrees in electrical engineering from the University of Paderborn, Paderborn, Germany, in 1993 and 1998, respectively.

From 1993 to 1998, he was a Scientific Research Assistant at the Institute for Power Electronics and Electrical Drives, University of Paderborn. His research interests were focused on power supplies and control strategies for piezoelectric drives. Since 1998, he has been with the Laboratory for Power Electronics and Actuators, DaimlerChrysler AG Research and Technology, Frankfurt, Germany, developing novel mechatronic actuator systems to improve the ride comfort of automobiles.



Thomas Schulte was born in Detmold, Germany, in 1970. He received the Dipl.-Ing. degree in electrical engineering in 1998 from the University of Paderborn, Paderborn, Germany, where he is currently working toward the Ph. D. degree in the Department of Electrical Engineering and Information Technology, Institute for Power Electronics and Electrical Drives.

He is also currently a Research Assistant at the University of Paderborn, working on controllers and power supplies for piezoelectric motors. His interests are control systems, digital control, piezoelectric drives, and new actuators.



Norbert Fröhleke was born in Paderborn, Germany, in 1951. He received the B. Sc. degree in electrical engineering from the University of Paderborn, Paderborn, Germany, the M.S. degree from the Technical University of Berlin, Berlin, Germany, and the Ph.D. degree from the University of Paderborn in 1975, 1984, and 1991, respectively.

He has worked in the fields of numerical control of tooling machines, electronics maintenance of electrical power stations, and teaching from 1976 to 1978 and in the field of power electronics from 1983 to 1984 at the former AEG. Since 1989, he has been coordinating the research activity in power electronics, supervising a large number of B.Sc./M.Sc. students, and performing the acquisition of projects in the Department of Electrical Engineering and Information Technology, Institute for Power Electronics and Electrical Drives, University of Paderborn, where he has also lectured. His research interests include switched-mode power converter analysis, modeling and control for various applications, high-frequency magnetics, and computer-aided development of power electronic circuits and magnetic components, piezoelectric drives, and new actuators.